actuators

MDPI

Article

Optimization and Experimental Investigation of a Single-Actuation Compliant Morphing Trailing Edge for Multiple Aerodynamic Configurations

Martynas Lendraitis * and **Vaidas Lukoševičius**

Faculty of Mechanical Engineering and Design, Kaunas University of Technology, Studentų Str. 56, 51424 Kaunas, Lithuania
* Correspondence: martynas.lendraitis@ktu.lt

Abstract

This work presents a low-fidelity optimization method for a compliant morphing wing trailing-edge structure, developed to achieve multiple optimized aerodynamic shapes under combined aerodynamic and control loads using a single actuation pathway. Typically, multiple shape configurations are avoided due to conflicting structural requirements that increase optimization complexity. To address this, a parameterization method based on practical considerations of compliant trailing-edge structures is introduced. A particle swarm optimization algorithm is employed, with multi-objective criteria handled through a penalty-based approach. The algorithm is demonstrated by optimizing the trailing edge for one and two aerodynamic configurations with high accuracy, achieving typical shape deviations of 0.04% and 0.08% relative to the chord for two shapes, and as low as 0.023% for a single shape. Several compliant structures are generated, manufactured, and tested for shape accuracy, including in a wind tunnel to evaluate aerodynamic performance. Experimental investigations confirm the feasibility of achieving two aerodynamic shape configurations with a single structure and show that the proposed methodology can improve the lift-to-drag ratio of a wing section with a deflected compliant trailing edge by more than 12.4% compared to conventional flaps at the same deflection.

Keywords: morphing trailing edge; flap; compliant structure; topology optimization; trailing edge

check for updates

Academic Editor: Ignazio Dimino

Received: 30 August 2025
Revised: 28 September 2025
Accepted: 13 October 2025
Published: 15 October 2025

Citation: Lendraitis, M.; Lukoševičius, V. Optimization and Experimental Investigation of a Single-Actuation Compliant Morphing Trailing Edge for Multiple Aerodynamic Configurations. *Actuators* **2025**, *14*, 498. https://doi.org/10.3390/act14100498

1. Introduction

Morphing structures have long been of interest in aviation, with numerous concepts reviewed in multiple articles [1–4]. A particularly promising approach is the use of compliant structures. Unlike conventional mechanisms with moving joints, monolithic compliant structures can achieve the desired shape changes solely through material flexibility. This reduces design complexity, lowers part count, and decreases manufacturing and maintenance costs [5,6]. Compliant structures can be applied either to a specific portion of a wing or to the entire wing [7,8]. Although full-wing morphing may be appealing from a research perspective, a more practical approach is to implement these structures only on selected sections, such as the leading [9,10] or trailing edge [11,12], while retaining a conventional design for the remainder of the wing.

Although compliant structures have their benefits, the main difficulty lies in obtaining a structure capable of morphing into the desired shape. Several methods exist for developing compliant morphing structures, ranging from relatively simple load-path approaches [13,14] to high-fidelity optimization techniques, such as BESO or level-set methods [15]. Low-fidelity methods offer fast computation, whereas high-fidelity approaches are more precise but complex and time-consuming. Intermediate methods also exist, often employing two-step optimization strategies, such as those used by Zhang [16]. Interestingly, the resulting structure patterns suggest that continuum theory used in high-fidelity optimizations may not be strictly necessary, as the final structures resemble multiple trusses and frames, which could initially be modeled using simplified approaches. Similar conclusions were drawn by [17]. However, empirically based optimization solutions remain underexplored, and further research in this area could be highly beneficial, as they would allow designers to obtain practical solutions more easily.

Analysis of several small-scale morphing compliant trailing-edge structures (with chord less than 0.3 m) reveals common structural features. Fasel [18] and Moulton [19] based their designs on empirical geometry and design without aerodynamic optimization, while Jia [20] and Tong [21] used high-fidelity topology optimization techniques to obtain a previously defined aerodynamic shape that would be achieved under actuation as illustrated in Figure 1. These designs feature continuous top and bottom trailing-edge surfaces connected by thin transverse straight or curved elements. These transverse elements provide additional stiffness to the outer skin, enabling supporting compliance and assisting outer surfaces during morphing. Such patterns are also observed in other compliant trailing-edge structures [22–24], suggesting that this feature could be used in the development of a parameterization algorithm.

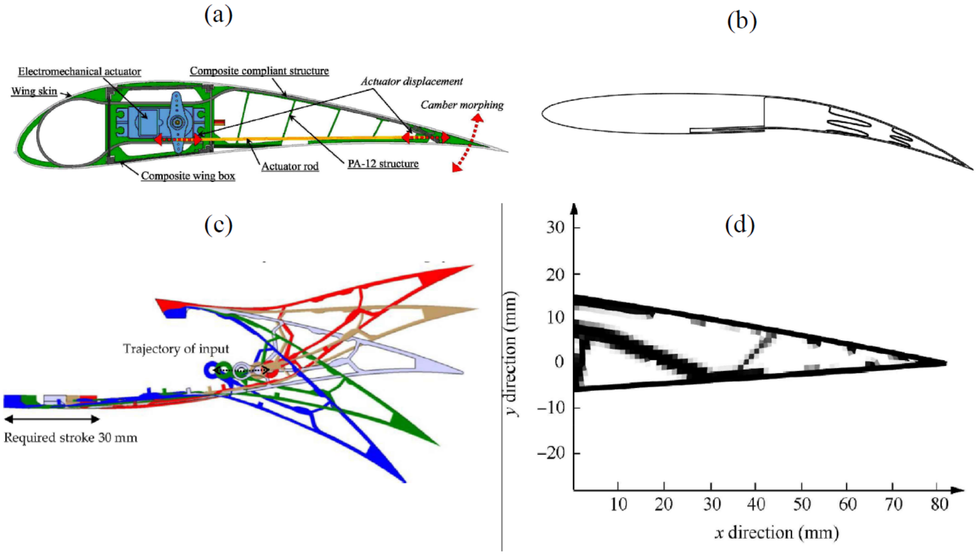

Figure 1. Compliant morphing design examples: (**a**) by Fasels [18], (**b**) by Moulton [19], (**c**) by Jia [20], and (**d**) by Tong [21].

Additionally, most compliant morphing structures currently consider only one target shape, restricting the achievable performance. Some researchers [24] have investigated intermediate deflections of the initial geometry for aerodynamic evaluation. This approach might not always give the best results, as intermediate shapes can be suboptimal and degrade or limit overall aerodynamic performance. Multicondition performance can be achieved using compliant structures with several layers of compliant elements [25], which would enable greater flexibility through multiple actuation pathways; however, practical considerations complicate such designs. Only recently have researchers achieved multiple configurations with a single structure and single actuation pathway (single actuator), optimizing for both upward and downward aileron (flap) deflection [26]. The proposed method is multilayered and robust, yet complex. Based on the results obtained from the research, it appears that the investigated morphing structure exhibits the structural features highlighted earlier, indicating a promising direction for parameterization development.

Building on these insights, the present work proposes a low-fidelity parameterization approach inspired by findings from the previously reviewed studies and the observations highlighted earlier. The method implements a parameterization of the trailing-edge structure, defined by variations in outer skin thickness and spline-based internal structures spanning from the upper to the lower surface, thereby supplementing the structure in morphing. It incorporates geometrically nonlinear beam analysis for rapid structural evaluation, applies constraints through parameterization, and employs a particle swarm optimization algorithm with multi-objectivity handled via a defined penalty function to address the conflicting outcomes of multiple aerodynamic shapes. Parameterization limits the boundaries of structural optimization, keeping the search within a practical design domain and speeding up the optimization process.

2. Materials and Methods

The proposed low-fidelity parameterization of the compliant trailing-edge structure consists of two main components: the outer skin formulation and the inner supporting structure formulation, both of which are parameterized. This approach enables the geometry to be defined with a small number of variables, thereby reducing optimization complexity. The outer skin and inner structure are determined based on practical considerations to maintain a simple overall geometry, while still allowing the generation of sufficiently complex shapes required for morphing. For structural evaluation, the trailing edge is represented as an assembly of finite element beam elements with varying cross-sectional properties, which further simplifies the analysis.

A key aspect of the parameterization lies in defining how the structure behaves through boundary conditions. For the trailing edge, the boundary conditions are set to create a compliant structure with a seamless, rigidly connected top skin and an actuated lower skin in the chord-wise direction. The actuation is initiated through a pulling/pushing motion on the leading portion of the lower skin Figure 2. Through this pushing/pulling motion, the structure's trailing edge is intended to deflect according to the actuation direction. The overall behavior, influenced by the skin and internal structure, is intended to be determined during optimization.

The upper trailing-edge surface remains continuous and fixed to the wing's main structure, whereas the lower surface at the actuation point is supported by a slider constraint. This constraint restricts motion perpendicular to the chord and prevents rotation but allows translation along the chord. In this formulation, trailing-edge morphing is initiated by applying a displacement constraint at the control rod position. This displacement acts as a design variable and one of the optimization parameters. Displacement, rather than force, is used to drive the trailing-edge morphing during optimization because displacement bounds are easier to control. By appropriately selecting these bounds, structural shape deformations can be effectively limited in unfeasible directions.

The compliant trailing-edge structure features an outer skin with spatially varying thickness. The outer trailing-edge surfaces are generated from airfoil coordinates, which serve as the base geometry. For surface parameterization, the thickness distribution is defined by m linearly spaced variables t_m, assigned along both the upper and lower trailing-edge surfaces. These variables are separated into upper surface values $t_1^u, t_2^u, \ldots, t_m^u$ and lower surface values $t_1^l, t_2^l, \ldots, t_m^l$ (Figure 2). The thickness parameters are used to construct a continuous curve which, when combined with the outer surface curve, defines the skin thickness distribution of the morphing trailing edge. While the external shape of the trailing edge remains unchanged, the prescribed thickness values are directed inward, thereby shaping the internal thickness profile of the structure.

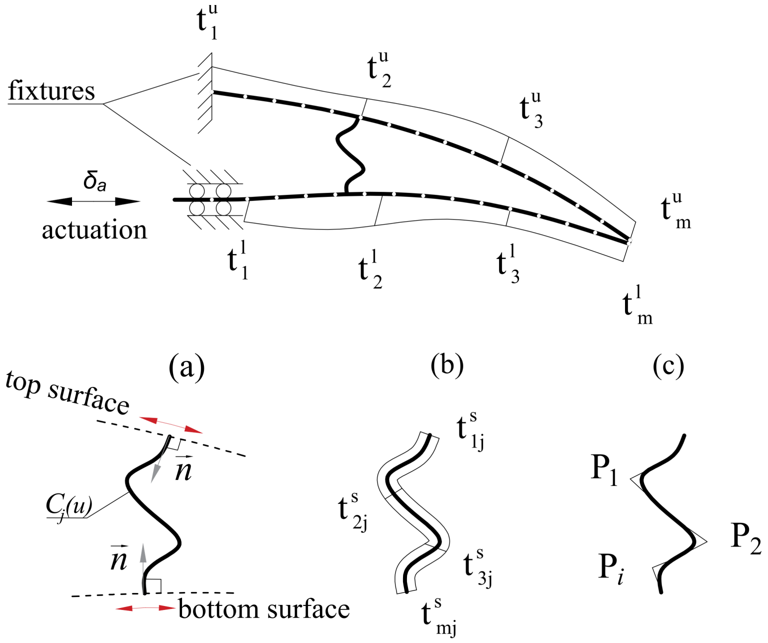

Figure 2. Top image: Setup for optimization, showing boundary conditions and thickness distribution on the top and bottom trailing-edge surfaces (thickness variation shown outward for clarity; in the algorithm, the outer surface is fixed and variations are shifted inward). Bottom image: Support structure represented by a spline. (**a**) Boundary conditions and initial-position variation on top/bottom surfaces; (**b**) thickness variables; (**c**) spline control variables.

The continuous inner surface boundary is formed using a Makima interpolation algorithm [27], denoted as the function $M(t, x)$. This interpolation approach mitigates the large overshoots typically associated with conventional splines, ensuring a smoother and more accurate representation. Based on the interpolated description, the structure is discretized into finite elements by mapping the thickness values onto the structural elements through interpolation, according to the center position of each element x_n:

$$\begin{aligned} t_n^u &= M\big(\{t_m^u\},\, x_n\big), \quad n = 1,\dots,n_{tot}^u,\\ t_n^l &= M\big(\{t_m^l\},\, x_n\big), \quad n = 1,\dots,n_{tot}^l. \end{aligned} \tag{1}$$

In this way, each element is assigned a constant thickness. Although the actual thickness distribution varies continuously along the element, the finite element evaluation algorithm used in the implementation requires all elements to maintain constant thickness.

The inner support structure serves as the backbone of the proposed method. It connects the upper and lower surfaces through arbitrarily shaped, spring-like elements. These elements provide reinforcement to the outer trailing-edge skin during large deflections and under significant aerodynamic loading, preventing the surfaces from moving excessively toward or away from each other. Similar support patterns are observed in multiple generated compliant structures, suggesting that including such a feature could provide an optimization shortcut. By improving the compliant characteristics of the trailing edge, the support structure helps to achieve the desired outer shape when actuated.

The geometry of the support structure must be precisely defined and is governed by several factors, including the target trailing-edge shape, the stiffness distribution of the outer surface, and the aerodynamic loading. Consequently, both the shape and placement of the support structure need to be optimized to achieve the desired performance.

The proposed method for defining the shape of an arbitrary support structure involves using splines to represent its geometry. In particular, a cubic B-spline curve, denoted as $C_j(u)$ is employed. The formulation of the support structure geometry is shown in Figure 2a–c, illustrating support structure geometry alterations such as the initial position variation, thickness, and general shape alteration through the control points. The support structure is always located inside the trailing edge, where the spline curve defining its shape starts on the top surface curve and ends on the bottom surface curve, producing an arbitrary shape in between. Boundary conditions are also imposed on the B-spline, requiring the curve to start and end perpendicular to the outer surface curves, with its tangent at the endpoints aligned with the surface normal to ensure that the spline remains within the structure:

$$\left.\frac{d\vec{C}_j(u)}{du} \times \vec{n}\right|_{u=u_0} = \vec{0} \quad \text{and} \quad \left.\frac{d\vec{C}_j(u)}{du} \times \vec{n}\right|_{u=u_{\text{end}}} = \vec{0} \tag{2}$$

The starting and ending positions of the B-spline are defined as a variable in the projected bounds to the upper and lower surface curve of the region $\Omega_{i,j}$. The shape of the B-Spline curve is controlled by a set number of control points $P_i(x,y)$. This directly defines how much the support structure can be modified: fewer control points limit control over the overall shape, while more control points increase variability and makes the optimization problem larger. The support structures can only be placed within the defined trailing-edge inner space $R(x,y)$, defined within the outer top $y_{\text{top}}(x)$ and bottom $y_{\text{bot}}(x)$ curves, though the trailing-edge length l_a:

$$R(x,y) = \left\{ (x,y) \in \mathbb{R}^2 \;\middle|\; 0 \le x \le l_a,\; y_{\text{bot}}(x) \le y \le y_{\text{top}}(x) \right\}. \tag{3}$$

Since multiple support structures can be defined within $R(x,y)$ space to prevent the splines from overlapping or intersecting the entire space is divided into a set of regions $\Omega_{i,j}$. Two types of regional divisions are used: vertical and horizontal. The vertical divisions are used to place all control points $P_i(x,y)$ of a single spline curve $C_j(u)$, while the horizontal divisions define the number of support structures j. The regions can be represented in matrix form, allowing any number of vertical and horizontal divisions to be specified:

$$\begin{bmatrix} \Omega_{1,1}(x,y) & \Omega_{1,2}(x,y) & \cdots & \Omega_{1,j}(x,y) \\ \Omega_{2,1}(x,y) & \Omega_{2,2}(x,y) & \cdots & \Omega_{2,j}(x,y) \\ \vdots & \vdots & \ddots & \vdots \\ \Omega_{i,1}(x,y) & \Omega_{i,2}(x,y) & \cdots & \Omega_{i,j}(x,y) \end{bmatrix} \tag{4}$$

where the columns are vertical divisions, and the rows are horizontal divisions. Graphically, the regions can be arranged within the design space of the trailing edge, as illustrated in Figure 3. The entire inner space of the trailing edge cannot be used, as the available vertical space gradually decreases toward the rear section, leaving insufficient room to accommodate the support structure. Therefore, the $\Omega_{i,j}$ regions are set at a x boundary from the beginning of the trailing-edge optimization region to the distance l_b. The horizontal trailing-edge space filling ratio is defined as the ratio between the length and the region boundary, expressed as $\frac{l_b}{l_a}$. The larger the trailing edge, the more space can be allocated for defining support structures.

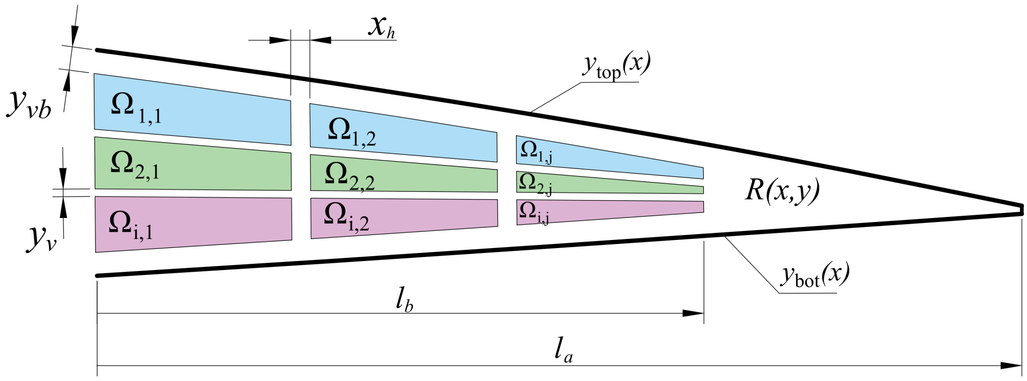

Figure 3. Design space, regions for control points, and buffer zones defined within the initial trailing-edge geometry.

To prevent the spline curves from intersecting, buffer spaces are established between the regions. The y_v is the vertical buffer and x_h is the horizontal buffer between the regions. A buffer region y_{vb} at the surface boundaries is also defined. This space is allocated to accommodate the outer surface thickness and, like other buffers, prevents the spline from crossing the outer surface. Therefore, it is larger than y_v. Taking into account these buffers, each region $\Omega_{i,j}$ is defined within R. For each vertical slice in between top $y_{\mathrm{top}}(x)$ and bottom $y_{\mathrm{bot}}(x)$ curves is divided into I number layers:

$$y_i^-(x) = y_{\mathrm{bot}}(x) + y_{vb} + \frac{i-1}{I}\Big[\big(y_{\mathrm{top}}(x) - y_{vb}\big) \;-\; \big(y_{\mathrm{bot}}(x) + y_{vb}\big)\Big], \quad i = 1, \ldots, I+1. \tag{5}$$

then the placement of every region $\Omega_{i,j}$ in space R can be expressed as

$$\Omega_{i,j} = \left\{ (x,y) \in R(x,y) \;\middle|\; \begin{array}{l} x_{j-1} + x_h \;\le\; x \;\le\; x_j - x_h, \\ y_i^-(x) + y_v \;\le\; y \;\le\; y_{i+1}^-(x) - y_v \end{array} \right\}. \tag{6}$$

These regions are used as upper and lower boundaries to place the defined number of B-spline knots. In the algorithm implementation, the region $R(x,y)$ of arbitrary shape is expanded to a square region, simplifying manipulation through linear relations defined by the outer region bounds ($\Omega_{i,j}$). The $\Omega_{i,j}$ sets the minimum and maximum limits for the optimizer. Once these relationships are defined, the transformation is reversed through an inverse transformation function, producing bounds that conform to the inner geometry of the trailing edge. This is implemented in the algorithm using a gridded interpolant, which defines the transformation space and simplifies the handling of boundary regions. It should be noted that, in this approach, the buffer regions are scaled together with the geometry.

To form the support structure, the generated B-spline curve $C_j(u)$ is discretized into evenly distributed coordinates. These coordinates are then used to create n_{tot} elements. The thickness of the support structure also varies using a methodology similar to that used in the formulation of the outer structure. A set of thickness variables $t_1^s, t_2^s, \ldots, t_m^s$ is defined. Then, element thicknesses along the support structure curve $C_j(u)$ is obtained using Makima interpolation:

$$t_n^s = M\big(\{t_m^s\}, u_n\big), \quad n = 1, \ldots, n_{tot}, \tag{7}$$

Once generated, the structure can be analyzed using a finite element algorithm. Represented by simple one-dimensional beam elements, the model requires only a small number of elements, making it feasible to employ computationally intensive methods such as geometrically nonlinear beam formulations. With the specified boundary conditions, these methods allow the structure to be evaluated and its deformed shape determined. During the calculation, both the actuation displacement and aerodynamic loading, distributed across the outer surface, are applied. The aerodynamic loading is essential for the structure to achieve the required geometry under the defined flight conditions. The aerodynamic loading at the defined speed V_{load} can be obtained using various CFD approaches, depending on the trailing-edge geometry and flight conditions. In this work, two-dimensional CFD simulations using the SST Transition turbulence model were carried out to provide the necessary pressure distribution data for the algorithm. As the main focus of the article is on the algorithm, the CFD setup is outlined in more detail in the validation of the algorithm section.

To evaluate the discrepancy between the desired and obtained trailing-edge shapes, the upper and lower surfaces are compared independently, requiring them to be separated. The discrepancy area A_{tot} is calculated as the total area between the two curves via integration, taking only absolute values, and is incorporated directly into the objective function, providing a measure of optimization fitness that naturally approaches zero as the shapes converge.

After the total area between the curves is determined, the average surface deviation can be obtained by dividing this area by the total length of the morphing surface. Since the discrepancy area forms the basis of the optimization evaluation, the corresponding average deviation is also reported alongside the results to provide clearer physical meaning.

2.1. Optimization Objective

The optimization is set up using particle swarm optimization to enable a broad global search. The optimization problem is formulated as unconstrained, with constraints incorporated into the objective function using a penalty method. Penalties, multiplied by the discrepancy area and the penalty coefficients $\lambda_1, \lambda_2, \lambda_3$, are adjusted according to constraint importance. Constraint values are also scaled by the discrepancy area, ensuring penalties remain of similar order. The constraints on discrepancy are only applied under certain conditions: when the maximum stress in the structure σ_{max} exceeds the allowable stress σ_{all}, when the computed flutter speed V_{fl} falls below the allowable flutter speed V_{f_all}, and when the actuation force F_δ exceeds the allowable actuation force $F_{\delta\mathrm{all}}$. The objective function is then expressed as

$$\text{Minimize}\begin{cases} A_{tot} \\ +\lambda_1 A_{tot}\max(0, \sigma_{max} - \sigma_{\mathrm{all}}) \\ +\lambda_2 A_{tot}\max(0, V_{\mathrm{f\_all}} - V_{\mathrm{fl}}) \\ +\lambda_3 A_{tot}\max(0, F_\delta - F_{\delta\mathrm{all}}) \end{cases} \tag{8}$$

For multi-objective optimization involving several aerodynamic target curves, the overall discrepancy A_{tot} is quantified by summing up the discrepancy areas corresponding to different actuations.

2.2. Algorithm Implementation

The structure formation and optimization algorithm was developed in-house using MATLAB R2024a. The main program includes inner functions that perform initial tasks such as generating the computational domain, forming boundary conditions, calculating initial actuation displacements, and more. The overall algorithm evaluation sequence is shown in Figure 4.

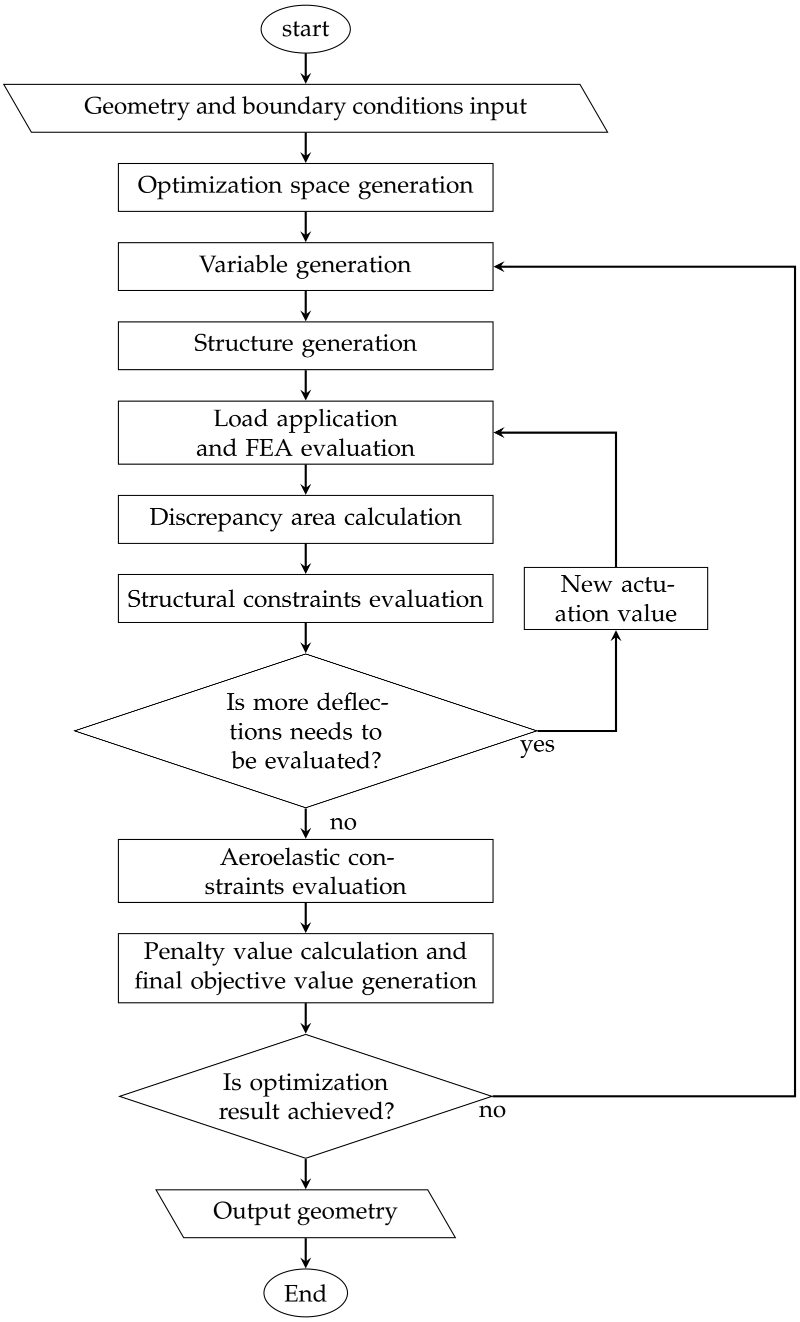

Figure 4. Block diagram illustrating the optimization algorithm for the compliant trailing-edge structure, showing the main steps and flow of the optimization process.

Within the program, structural calculations are performed using the MATLAB-based NUMA-TF program [28]. This program performs nonlinear numerical calculations of trusses and frames. It is integrated into the main objective evaluation program and runs in batch mode, evaluating the given structure and outputting deformations, element forces, stresses, and strains. Only the initialization of the control sequence in the main NUMA-TF program is modified, leaving the core evaluation code unchanged to preserve the program logic. It is set such that all morphing-shape analyses would use the geometrically nonlinear Timoshenko beam theory formulation. The thickness of the beam elements was determined by the parameterization algorithm, with additional modifications made to the cross-sectional properties of the beam element before evaluation.

Although the beam geometry could employ a rectangular cross-section, it is modified to accommodate the specific manufacturing method, namely FDM 3D printing. The cross-sectional area and second moment of area are adjusted to account for the surface irregularities on the outer sides of 3D print, which are typical of FDM printing.

Printing the structure vertically on the print bed allows for an almost continuous variation in the thickness of the printed compliant trailing-edge geometry. This is achieved by placing the outer raster paths at precise positions on the bed and filling the inner areas with the remaining material. To further refine thickness control, the extrusion rate of the filament is adjusted using the Arachne slicing method, as described by [29], which enables precise, adaptive variation of perimeter widths during printing.

In 3D printing, the resulting material is not fully homogeneous, and its strength and stiffness are strongly influenced by the printing parameters and raster orientation [30]. To achieve more consistent mechanical properties, the slicing of the morphing compliant trailing edge is designed so that the rasters extruded on the print bed are aligned with the geometry of the trailing-edge structure, with each subsequent layer placed directly above in the same orientation. This produces a material that can be approximated as transversely isotropic, with variations primarily governed by the cross-sectional geometry.

Vertically printed samples exhibit ridged side surfaces formed by semi-circular bulges, which are mainly determined by the nozzle width and layer height. A model of this cross-section, whose properties are applied to the beam, is developed from Scanning Electron Microscope (SEM) images of cuts of similar printed samples, incorporating parameters such as layer height, nozzle width, and number of layers on the bed with variation of perimeter width. The relevance of these cross-sectional properties to the section model is further addressed in the Discussion section.

Force constraints are directly computed via FEM analysis, and aeroelastic constraints are assessed using a low-fidelity method. In this procedure, the equivalent stiffness of the unactuated structure is determined using FEM and incorporated into the well-established Theodorsen typical section model [31]. This model is characterized by typical section parameters such as the heave stiffness K_h, torsional stiffness K_θ, the mass per unit span m_w, the mass moment of inertia I_θ, and fixed geometrical properties x_θ and a. The flap torsional stiffness is determined considering actuation system stiffness K_δ. The model is resolved using the p-method to ensure the structure remains flutter-free under specified conditions. Similar strategy has been employed by other researchers [32]. This method allows for a rapid assessment without excessive computations, as more detailed analysis would need to follow in subsequent design stages. Nevertheless, it maintains acceptable reliability in the initial optimization phase with an adequate safety margin.

The algorithm is designed so that various optimization methods can be easily implemented. In this work, only limited evaluations on the selection of the optimization algorithm were performed, so detailed research was not included in the article. These evaluations are focused on three different stochastic algorithms, TLBO, GA, and PSO, which requires multiple runs to reliably assess their performance for the particular problem. Each algorithm is run 50 times for three different population sizes using predefined parameters and a fixed 10,000 function evaluation count. The particle swarm optimization algorithm from the MATLAB Global Optimization Toolbox is selected for this research, as it shows the most promising results during algorithm evaluation. It achieves the lowest mean objective function value, approximately 8% lower than the second-best TLBO algorithm, while maintaining a similar standard deviation at the end of evaluation.

The selection of key parameters in the final optimization is guided by a sensitivity analysis involving multiple runs and statistical evaluation. For the present case, an additional isolated study is conducted by varying parameter settings and assessing their effect on the objective function. Due to the stochastic nature of the PSO algorithm, each configuration is evaluated 100 times. The results indicate that two support structures with

2–3 vertical divisions perform best, while outer surface thickness parameters are most effective when their number exceeds 10. Buffer sizes are not explicitly analyzed but are defined with respect to the established thickness boundaries. Additional details on the algorithm and parameter selection are available from the authors upon request.

3. Validation of the Algorithm

For the investigation of the algorithm, several validation cases are considered. The first case evaluates the algorithm's ability to generate the required optimized shape. This is assessed both through the algorithm's numerical output and through experimental testing of the manufactured structures. The second validation case focuses on aerodynamic performance, where the manufactured trailing-edge flap sections are integrated into a wing and tested in a wind tunnel. The results are compared with CFD predictions and with those of a conventional plain type flap. The aerodynamic shapes of the trailing edge analyzed in this study are generated using an aerodynamic shape generation algorithm as described in [33] which uses XFOIL for performance evaluation. This algorithm employs a shape parameterization method with compliant shape constraints, ensuring better alignment of the generated shapes with the behavior of the compliant morphing trailing-edge structure. This approach provides the structural formation algorithm presented in this paper with a more robust foundation for achieving the desired geometries.

3.1. Aerodynamic Shape Generation and Set Up for Shape Accuracy Investigation

The NACA 2412 airfoil is selected as the baseline for optimization. Several trailing-edge aerodynamic shapes were generated through optimization under defined settings, with the morphing starting location fixed at $0.6c$, where c denotes the wing chord. For aerodynamic evaluation during optimization, XFOIL Version 6.99 is configured with standard settings, using an Ncrit value of 9 and 200 panels. The first aerodynamic optimization case is aimed to maximize the lift-to-drag ratio in the section lift coefficient c_l range between 0.7 and 1.0 at a Reynolds number of 500,000. This was achieved at $-0.038c$ trailing-edge displacement, which is defined in reference to the chord c. The second aerodynamic optimization is aimed at achieving maximum lift on a set trailing-edge deflection of $-0.1c$. In the second deflection shape optimization, specific measures are implemented to enhance the optimization outcome. To achieve a shape similar to the first optimization, the resulting geometry from the initial optimization us used as a starting geometry, which is then further deformed to reach a trailing-edge deflection of $-0.1c$. More details on the method can be found here [33]. The resulting aerodynamic shapes from both optimizations are shown in Figure 5.

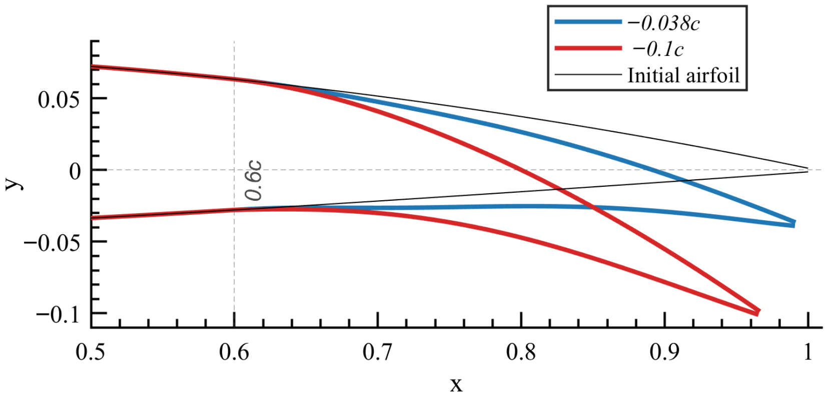

Figure 5. Aerodynamically optimized trailing-edge outer geometry, at $-0.038c$ and $-0.1c$ trailing edge displacement.

The structural optimization to form the compliant structure is performed on a wing section with a chord length of 0.5 m and a width of 0.01 m, using homogeneous PC-blend polycarbonate plastic as the structure material with an experimentally determined Young's modulus of 2.34 GPa. For this optimization, two supporting structures are used, with the spline control points of each structure set to three. The top and bottom surfaces are defined with ten thickness variables. The optimization is constrained by a maximum allowable stress σ_{all} of 42 MPa and a maximum actuation force $F_{\delta \text{all}}$ of 10 N. Aerodynamic loading and aeroelastic evaluation are excluded from this optimization, as the structures are intended for static testing only. The thickness t of the structural elements and the actuation displacement δ_a bounds are shown in Table 1.

Table 1. Main structural boundaries for optimization of a morphing trailing edge in meters.

	Skin	Inner Structure		Actuation Displacement	Second Actuation Displacement
t_{min}	0.00045	0.00045	$\delta_{a\,\text{min}}$	−0.005	−0.012
t_{max}	0.003	0.003	$\delta_{a\,\text{max}}$	−0.004	−0.011

For structural calculations, the upper and lower surfaces are divided into 41 beam elements, while each supporting structure is divided into 10 beam elements, resulting in a total of 61 elements within the optimized structure. The optimization is carried out using a particle swarm optimization (PSO) solver with a swarm size of 50 individuals and is manually stopped after 200 iterations. This setup is chosen to keep the optimization relatively fast, using only 10,000 function evaluations per optimization.

Using aerodynamic shapes as the main objective, two different optimized structures are generated using the algorithm presented in this paper. One structure is generated to achieve only a shape with trailing-edge deflection of $-0.038c$, while another is designed to achieve both $-0.038c$ and $-0.1c$ deflections at different actuation inputs. The obtained complaint structures are seen in Figure 6. Interestingly, in the generated structures, geometry (a) features a thicker outer surface on the upper side, whereas in geometry (b) the thicker surface shifts to the lower side. Both geometries are optimized to reach the same shape at the first actuation displacement. This highlights the influence of the supporting structure in achieving the final geometry.

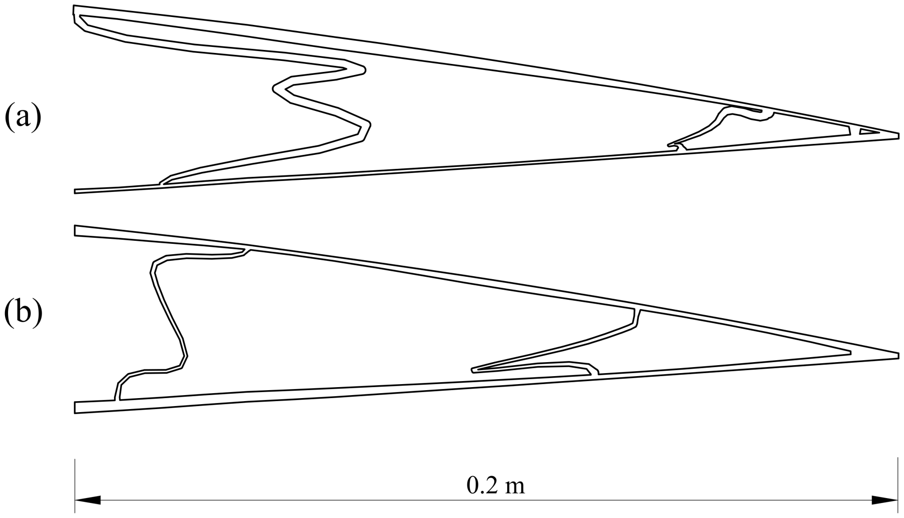

Figure 6. Structures optimized to achieve either one or two aerodynamic shape geometries: (**a**) achieves single shape, (**b**) achieves two shapes.

Figure 7a shows the discrepancy areas of the structure achieving single aerodynamic shape, with the top surface filled in pink and the lower surface in blue. The solver achieves a minimum discrepancy area of $4.54 \cdot 10^{-5}$ m^2, with the discrepancies appearing mainly along the shape boundaries, indicating that the optimization reproduces the target geometry very closely. To quantify the average deviation from the intended geometry, the discrepancy area is divided by the total length of the trailing-edge boundary, resulting in $1.125 \cdot 10^{-4}$ m for this case.

The same optimization setup is applied for structure aiming to achieve two configurations at different actuation inputs. An additional variable is introduced to control the second actuation displacement, enabling the formation of a second geometry. The optimization objective is defined as the sum of the individual objectives for each shape. The optimization converges to a discrepancy area of $1.97 \cdot 10^{-4}\,\mathrm{m}^2$ for the first shape and $5.92 \cdot 10^{-5}\,\mathrm{m}^2$ for the second. In this optimization, the discrepancies between the two configurations are not equal. The second shape is achieved with significantly higher accuracy, whereas the first one has noticeably poorer results. This highlights the challenge of optimizing two geometries simultaneously, as it may require compromises. Since the optimization is guided by fixed coefficients in the penalty function, the solution converges toward the best overall output, rather than yielding more balanced designs that could be obtained from a Pareto approach. However, the resulting shape achieves a reasonably good fit to the desired geometry as can be seen in Figure 7b,c.

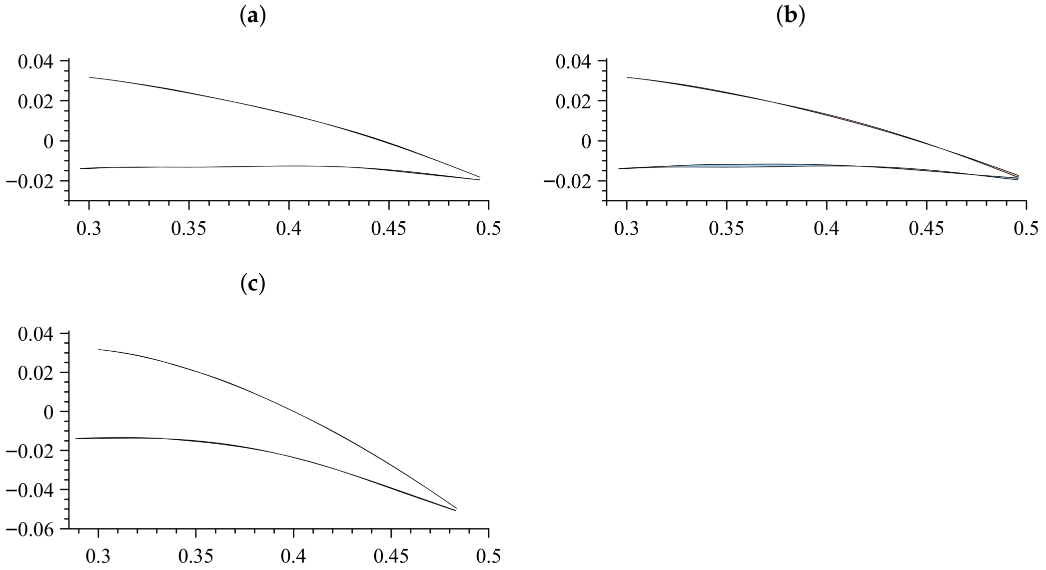

Figure 7. The discrepancy area is shown as the shaded region between the desired and obtained curves of morphing structures: (**a**) single morph structure; (**b**) double morph structure-first achieved shape; (**c**) double morph structure-second achieved shape.

The optimized structures are manufactured using 3D printing. Since the algorithm generates only 2D sections, the sample wings are extruded to a height of 0.01 m as used in the optimization setup, to obtain three-dimensional test specimens. In addition, a fixture is designed to position the structures within the actuation rig, accurately reproducing the boundary conditions applied during optimization (Figure 8). The samples are manufactured using the Prusa MK3 3D printer, equipped with a 0.4 mm nozzle and an enclosure to maintain a stable temperature during printing. The slicing patterns are generated using PrusaSlicer 2.6 software, configured so that the extruded filament aligns with the structure to produce a nearly transverse isotropic material. This is achieved by laying extrusions along the structure boundary, where the filament is continuously placed as layers (perimeters) to fill the entire structure. Such a placement allows for more homogeneous mechanical properties, closer to those assumed in the finite element algorithm.

The manufactured wing samples are then mounted on a linear actuation rig, which allows precise motion control via a lead screw. For preliminary actuation, electronic calipers are attached and used for initial placement. Measurements are performed on a Mitutoyo coordinate measuring machine equipped with a touch probe and a laser scanner. The measurement precision of the equipment is specified as MPE = (1.7 + 0.3L/100) µm, where L denotes the measured length in millimeters. The main non-touch surface measurements are performed with an Mitutoyo SM 606 laser scanner, which has a scanning error of 12 µm. The complete experimental setup is shown in Figure 8.

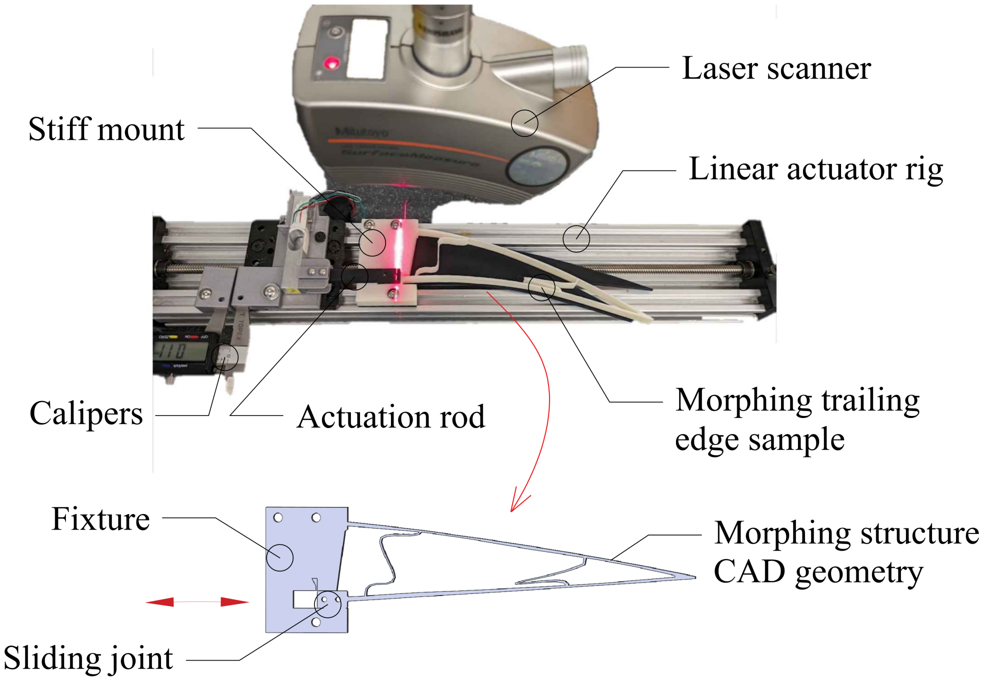

Figure 8. Outer shape scanning setup (**top**) with actuation rig. The (**bottom**) image shows the CAD geometry with the fixture and the compliant trailing-edge structure.

3.2. Shape Accuracy Results

The initial scan is conducted on an unactuated structure to identify the baseline discrepancy area error on manufactured compliant trailing edge. A laser scanning procedure is performed to collect the outer boundary coordinates of the trailing-edge sample, which is saved in a point cloud file. This file is then processed in software to extract the outer boundary curves, which are subsequently aligned with base points on the structure to ensure correct orientation and enable accurate comparison. After that, the discrepancy area is calculated between the resulting curves and the target curves. The single and double morphing flap samples achieve a similar base discrepancy area, around $50 \cdot 10^{-6}$ m^2. This corresponds to an average deviation of about 0.126 mm over the entire compliant trailing edge surface. Thanks to the careful calibration of the 3D printer and the used material, the base error aligns closely with the typical accuracy of FDM-type 3D printers, which usually falls between 0.1 and 0.3 mm.

Next, scanning is performed on the actuated (deflected) morphing trailing edges. A single morphing trailing-edge structure is actuated to the displacement determined from the optimization. The displacement is initially set roughly using calipers on the actuation rig, and then the trailing-edge displacement is verified and fine-tuned with a coordinate machine touch probe. Finally, the laser scanning procedure is performed to capture the outer boundary of the morphed shape.

The obtained discrepancy area and surface deviations are presented in Table 2. In the measurement case with laser scanner, the uncertainty for the discrepancy area in all test cases is $9 \cdot 10^{-6}$ with a confidence level of 95%. From the table, it is evident that the difference between the discrepancy values achieved in the optimization and the discrepancy area of the manufactured structure remains relatively stable when considering the base shape error. All resulting errors are comparable in magnitude to the shape error itself, indicating that the optimization process achieved high shape accuracy despite manufacturing imperfections. Notably, for the double-morphing wing sample, the first shape error closely matches the experimental result, even though the initial shape error is significant, suggesting some compensating overlap between errors that balance the outcome.

Table 2. Discrepancy area and average surface deviation obtained from FEM analysis and experimental measurements.

Discrepancy Area (10^{-6} m^2)				
Shape	**Algorithm**	**Base Error**	**Experimental**	
Single morph structure	45.45	50.62	112.61	
Double morph structure, 1st shape	197.89	49.43	191.45	
Double morph structure, 2nd shape	59.23	–	111.61	
Average deviation (10^{-3} m)				
Shape	**Algorithm**	**Base error**	**Experimental**	**Diff.**
Single morph structure	0.113	0.126	0.280	0.167
Double morph structure, 1st shape	0.492	0.118	0.476	0.008
Double morphs structure, 2nd shape	0.147	–	0.277	0.080

To better illustrate the data, a plot is generated to directly compare the algorithmic and experimental results along the chord-wise direction. As shown in Figure 9, the two results exhibit similar trends and a consistent pattern of discrepancies. This supports the accuracy of the findings and indicates that the structural formulation within the algorithm is both correct and reliable.

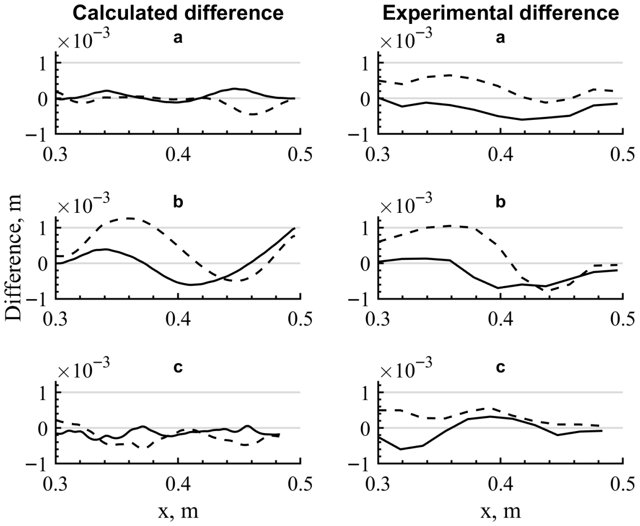

Figure 9. Comparison of local deviations between the target curve and the obtained geometries, from algorithmic results and experimental measurements. The solid line represents the upper trailing-edge surface, while the dashed line indicates the lower surface. (**a**) Single-morph structure. (**b**,**c**) First and second shapes of the double-morph structure, respectively.

3.3. Shape Generation and Set Up for Aerodynamic Evaluation

For wind tunnel testing, two other trailing-edge deflection cases are aerodynamically optimized: one deflects downward ($-0.05c$) and one upward ($0.05c$). The downward case is optimized for maximum c_l/c_d at 400,000 Re, while the upward case is aimed at minimizing section drag coefficient c_d. The angle of attack range for aerodynamic optimization is selected to represent hypothetical flight conditions at which the trailing edge would be actuated. A range of angles of attack is considered in the optimization to ensure that the overall aerodynamic geometry would not be optimized for a single operating point, which could otherwise result in impractical shapes and degraded performance across other flight conditions as stated in [34]. The Reynolds number is calculated using the planned wind tunnel model chord length of 0.26 m and a flow velocity of about 22 m/s. The resulting aerodynamically optimized flap geometries are shown in Figure 10.

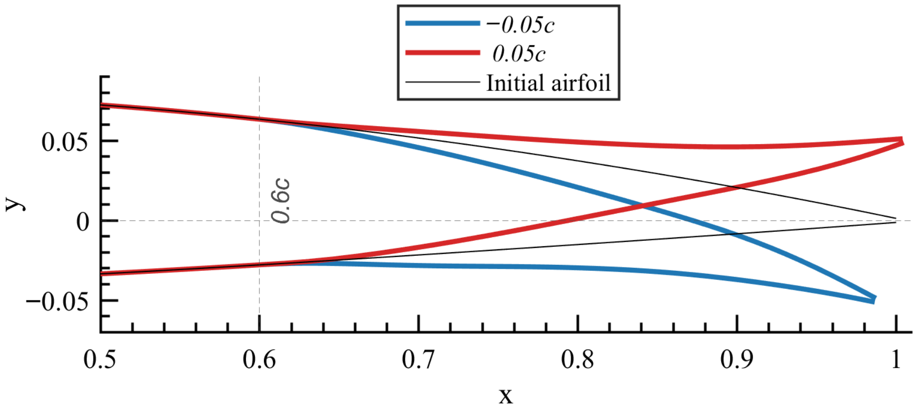

Figure 10. Optimized aerodynamic shapes at displacements of $-0.05c$ and $0.05c$.

The optimization is set up using the presented algorithm to define the inner structure of the morphing compliant trailing edge. Two support structures and fourteen outer skin thickness variables are selected based on previous findings to ensure effective structural definition. Optimization is performed for both actuated trailing-edge sections simultaneously, with a maximum actuation force of 4 N specified for a 0.01 m thick wing section. Other optimization settings are shown in Table 3. Most stiffness and mass properties needed for setup are chosen to closely match the experimental setup, preventing flutter or divergence during testing.

In this optimization, aerodynamic loading and aeroelastic constraints are considered. Both structural shapes are optimized for a single flight speed condition at 0° angle of attack. The optimization uses aerodynamic loading obtained from a CFD simulation at this angle, with trailing-edge deflections of $\pm 0.05c$. CFD simulations are performed with ANSYS Fluent 2024 R1 in 2D using the SST Transition model at 22 m/s. The SST Transition model is selected for its relevance to low Reynolds number conditions and its ability to predict drag accurately through precise flow transition modeling. For the CFD, a C-type flow domain is used, with a total length of $41c$ and a C-portion diameter of $16c$, both defined in chord length c. The airfoil surface boundary is divided into 1014 segments, each corresponding to elements approximately 0.52 mm in length for the full-size airfoil. A mesh inflation layer with 16 layers and a growth rate of 1.1 is applied at the boundary to ensure accurate boundary layer calculations. The C-shaped domain contains approximately 1 million cells. The mesh is resolved to have an y^+ value on the wings surface between 0.01 and 1, where $y^+ \leq 1$ is needed to ensure that the wall adjacent cell can accurately represent the flow characteristics in the laminar sublayer, to accurately predict the flow transition. The surfaces around and behind the airfoil are additionally refined with smaller elements. The surface roughness of the 3D-printed flap is not considered in the model since the printed rasters are aligned with the flow, making little difference in the 2D analysis.

Using a single flight speed to determine the aerodynamic loading for different trailing-edge deflections limits the optimization to that specific flight condition. As a result, the structure achieves the desired aerodynamic shape only under this condition. At other flight speeds, the structure might exhibit larger errors due to differences in aerodynamic loading.

Table 3. Optimization boundary conditions and constraint settings defined for generating the trailing-edge structure.

Wing Geometry		**Main Optimization Settings**		**Aeroelastic Settings**	
Parameter	**Value**	**Parameter**	**Value**	**Parameter**	**Value**
Span	0.26 m	Support struct. count	2	K_h	2000 N/m
Chord	0.26 m	Support struct. variab. count	3	K_θ	200 Nm/rad
Thickness	0.0312 m	Outer thic. variab. count	14	K_δ	40,000 N/m
Starting pos.	0.6c	Suppport struct. thic. variab. count	3	m_w	1 kg/m
		t_{min}	$5 \cdot 10^{-4}$	I_θ	0.005 kgm
		t_{max}	$3 \cdot 10^{-3}$	a	−0.1
		σ_{all}	42 MPa	x_θ	−0.22
		V_{load}	22 m/s	V_{f_all}	35 m/s

Using the same PSO algorithm as previously used with identical settings, the algorithm achieves a minimum discrepancy area of $3.36 \cdot 10^{-5}$ m^2, corresponding to a mean surface deviation of $0.16 \cdot 10^{-3}$ m across the trailing-edge surface. The trailing edge with downward deflection reaches a discrepancy area of $4.62 \cdot 10^{-5}$ m^2, corresponding to a mean deviation of $0.22 \cdot 10^{-3}$ m. The resulting geometry discrepancy area is shown in Figure 11. Most of the deviations across the trailing edge show good agreement; however, both shapes exhibit some areas with larger deviations caused by optimization compromises, which could impact aerodynamic performance. In general, the average deviations from the shape optimization are comparable to the capabilities of the FDM 3D printer, indicating that the achieved shape accuracy is acceptable. The geometry of the generated compliant trailing-edge structure is shown in Figure 12.

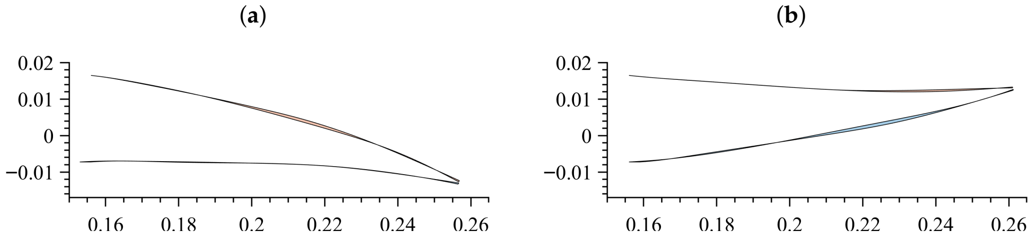

Figure 11. The discrepancy area is shown as the shaded region between the desired and obtained curves of the optimized morphing trailing-edge structure on a 0.26 m chord wing. (**a**) Downwards deflection $-0.05c$, (**b**) upwards deflection $0.05c$.

For wind tunnel testing, two sets of wings are manufactured: one that uses a conventional flap and the other, a morphing trailing-edge flap (Figure 13a). The wing equipped with a conventional flap serves as a benchmark to validate and compare the performance of the morphing trailing edge. The conventional flap is defined as a plain flap with its rotation axis located at the same position, 0.6*c* from the leading edge, corresponding to the beginning of the morphing region of the optimized trailing-edge structure.

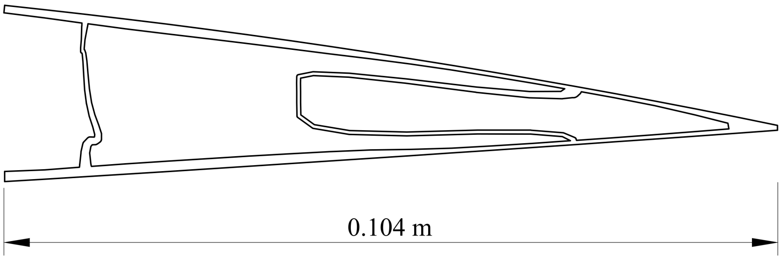

Figure 12. Optimized structure of a morphing trailing edge for manufacturing a wing intended for wind tunnel testing.

Discrepancies between wind tunnel results and theoretical calculations can arise from factors such as flow turbulence, static pressure variations along the test chamber, wind tunnel blockage effects, and measurement inaccuracies. Consequently, the most reliable performance evaluation is obtained by comparing the results of the two wings, each equipped with a different type of flap as presented here.

The test wings are manufactured using a combination of composite materials and 3D-printed components. The design features outer composite skins bonded to a 3D-printed internal structure that houses the servo motors, wing mounts, and steel mounting rod. Conventional flaps are attached via hinge at 0.6*c* from the leading edge, while the 3D-printed morphing structure is directly bonded to the wing with an additional stiffening component and a sliding joint. The implementation of the morphing trailing edge is shown in Figure 13b, with the control system and the structure of the morphing trailing edge visible.

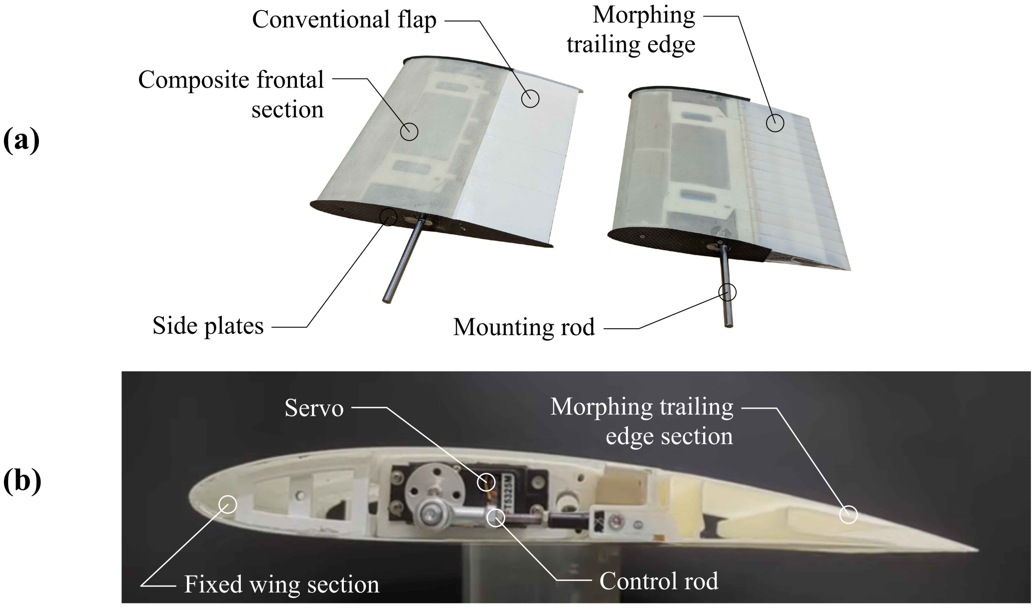

Figure 13. (**a**) Manufactured wings for wind tunnel testing with conventional and morphing trailing-edge flaps. (**b**) Side view of a wing with an optimized compliant morphing trailing edge and control servo.

The experiment is carried out in an AEROLAB wind tunnel with a working chamber dimensions of 0.295 × 0.295 × 0.6 m and the turbulence level is 0.2%. The test wings are designed to obtain section aerodynamic coefficients (2D); therefore, the wings are spanning the whole wind tunnel. The wings are also equipped with additional split plates to eliminate the boundary layer at the tips. Lift is measured directly using a force balance, while drag is determined from wake distribution measurements obtained with a movable Pitot tube placed 1*c* distance behind the wing trailing edge. All measurements are performed carefully and repeated multiple times. Lift measurements are carried out in five separate test runs. For each configuration, data are recorded for 5 s at a sampling rate of 1613 Hz, and the results are averaged before plotting. The standard deviation is calculated from the five independent runs. This procedure is applied to minimize potential systematic errors. Similarly, drag measurements are performed by capturing 50 readings in 5 s for each Pitot tube position while mapping the wake. The experimental setup in the wind tunnel's working chamber is shown in Figure 14.

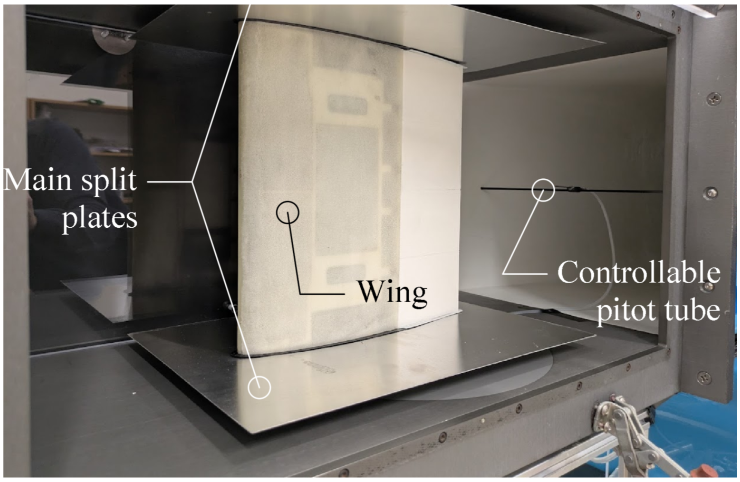

Figure 14. Wing with conventional flap inside the wind tunnel.

3.4. Aerodynamic Evaluation Results

Before testing, the wing is inspected in the wind tunnel at speeds slightly above the evaluation speed, up to 25 m/s, to check for flutter or divergence. No issues are detected, confirming that the aeroelastic limits are respected and that the tests can be safely carried out.

Two types of tests are conducted at a Reynolds number of 400,000. The first test includes four runs, two for each wing. In each run, both the conventional flap and the morphing trailing edge are fully deflected upward and downward. The tests are performed over an angle of attack range of −4° to +6°. The second type includes runs at fixed angles of attack of 0°, 2°, and 4°, with a full flap deflection sweep from $-0.05c$ to $0.05c$ to evaluate performance at intermediate deflections. The standard deviations for specific experiments are shown in Table 4.

Table 4. Standard deviation (std) values of c_l and c_d obtained from different experimental runs.

Experiment	Std $c_l \cdot 10^{-2}$	Std $c_d \cdot 10^{-4}$
Conventional flap, $-0.05c$	2.25	2.6
Conventional flap, $0.05c$	0.61	2.9
Morphing trailing edge, $-0.05c$	2.17	2.4
Morphing trailing edge, $0.05c$	0.90	2.8

After all wind tunnel measurements are completed, flow blockage corrections are applied to the obtained results. These corrections are obtained through CFD simulations, comparing the coefficients of the wing with the morphing trailing edge in free flow and within the wind tunnel, to account for nonlinear effects caused by the relatively large tunnel constrictions. The same blockage correction is applied to both the conventional and morphing wings to ensure that it does not affect the comparison of the results.

To verify the experimental results, they are compared with XFOIL and CFD predictions. XFOIL simulations are performed using standard settings at a Reynolds number of 400,000, with an Ncrit value of 9 and 200 panels, while CFD simulations are conducted in ANSYS in 2D using the SST Transition model at 22 m/s at the same Reynolds number using the same settings as described earlier.

The experimental and CFD results are compared for morphing trailing edge actuated upward (0.05*c*) and downward (−0.05*c*) (Figure 15a). Some discrepancies are observed between the two computational methods and the experimental results. For the downward-deflected trailing edge, the experimental data lay between the XFOIL and CFD predictions. In this case, the SST Transition model likely does not capture flow transition accurately and overestimates drag, resulting in the XFOIL prediction being closer to the experimental results. For the upward-deflected case, the experimental results show higher drag and slightly greater lift compared with both computational methods. Notably, in the actuated morphing trailing-edge configurations, the overall drag polar shape aligns more closely with the XFOIL prediction, despite its usual tendency to overestimate drag. Additional variations may arise from the wind tunnel setup and the morphing geometry itself. Some of the deviations could also be attributed to shape inaccuracies introduced by the optimization algorithm, as seen in Figure 11, as well as to manufacturing tolerances that may introduce slight geometric changes. A different choice of CFD model or settings, such as a finer mesh, might have produced more accurate predictions. However, some deviations from the experimental results are expected, as the simulations cannot account for possible geometric variations in the physical models.

Overall, the level of agreement is considered acceptable, as the final analysis relies primarily on the experimental data and the comparison between the conventional and morphing wing models. Testing both geometries in the same wind tunnel enables a direct evaluation of their performance, minimizing variations introduced by data acquisition methods and initial shape differences. At the same time, it captures genuine geometric variations arising from the compliant structure.

A direct experimental drag polar comparison between the conventional flap and morphing trailing edge is shown in Figure 15b. The drag polar clearly demonstrates the performance advantage of the morphing trailing edge. The objectives defined in the aerodynamic shape optimization are evident in the polar: a downward-deflected trailing edge generates more lift with significantly lower drag, resulting in a higher c_l/c_d ratio, while an upward-deflected trailing edge achieves substantial drag reduction with minimal impact on lift.

Overall, the experiments confirm the benefits of the compliant morphing trailing edge. Within the initially optimized angle of attack range of 0° to 4°, the optimized morphing trailing edge achieves a mean c_l/c_d of 87.4 for the downward-deflected (−0.05*c*) case, compared with 77.7 for the conventional flap, representing an improvement of approximately 12.4%. In addition, the morphing trailing edge reduces the average drag by approximately 9% compared to the conventional flap at this deflection.

For the upward-deflected (0.05*c*) morphing trailing edge, which is optimized for minimum drag, the mean c_d over the intended angle of attack range is 0.0109, representing a reduction of 16.8% compared to the conventional flap. This drag reduction results in a substantial improvement in aerodynamic efficiency under upward deflection, with the mean c_l/c_d increasing from −7.7 to −15.9.

These improvements exceed the initial XFOIL predictions, which estimated a c_l/c_d increase of 9.2% for the downward-deflected case and a drag reduction of 16.7% for the upward-deflected case. The actual improvement for the downward-deflected morphing trailing edge surpasses predictions by 3.2%, while the drag reduction for the upward-deflected case closely matches the predicted value.

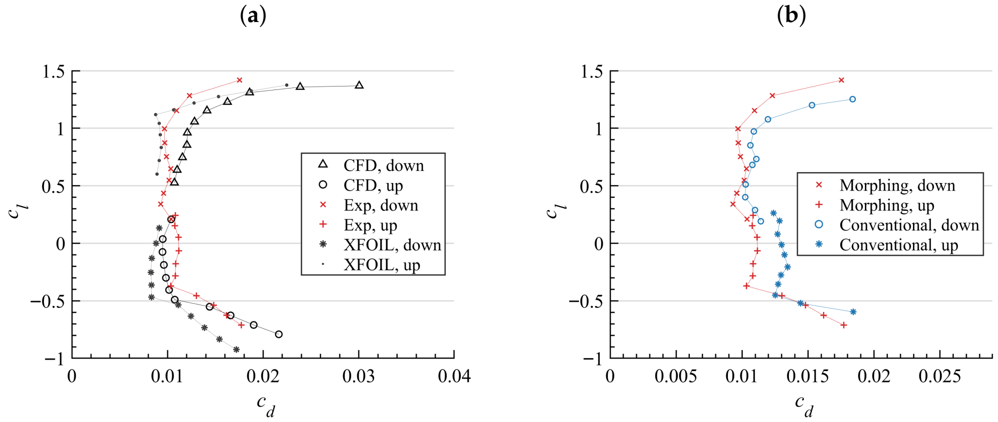

Figure 15. Comparison of drag polar results: (**a**) computation vs. experiment at −0.05*c* and 0.05*c* deflections; (**b**) morphing vs. conventional flap at −0.05*c* and 0.05*c* deflections.

The observed performance difference might be attributed to the morphing structure itself. XFOIL does not account for drag caused by the wing-flap junction, which can trip the flow and increase drag, nor does it accurately capture effects in cases of flow separation. In the manufactured wings,the wing with the morphing trailing edge has a smoother upper contour, whereas the conventionally flapped wing features a skin overlap at the hinge forming a seal, which may slightly influence its performance. This difference could explain why the experiments demonstrate a slightly greater performance increase than initially predicted for the morphing configuration.

In the second part of the experiment, intermediate deflection positions are examined by analyzing the performance of the conventional flap and morphing trailing edge. The trailing-edge displacement is varied from −0.05*c* to 0.05*c* in steps of 0.01*c*.

The wings are examined at three angles of attack, 0°, 2°, and 4°, for both the conventional and morphing configurations. Figure 16 illustrates how lift and drag vary with different flap and trailing-edge deflections. The graphs resemble wing-flap polars, when the angle of attack is held constant, and only the deflection varies. Different deflection angles are reflected in the corresponding lift coefficient values. Data points that nearly coincide represent the zero-deflection positions, where the performance is identical.

In most cases, the morphing trailing edge outperforms the conventional flap, primarily due to its consistently lower drag at each deflection. The only exception occurs at 0° angle of attack with a downward-deflected flap, where its performance is comparable to that of the conventional configuration.

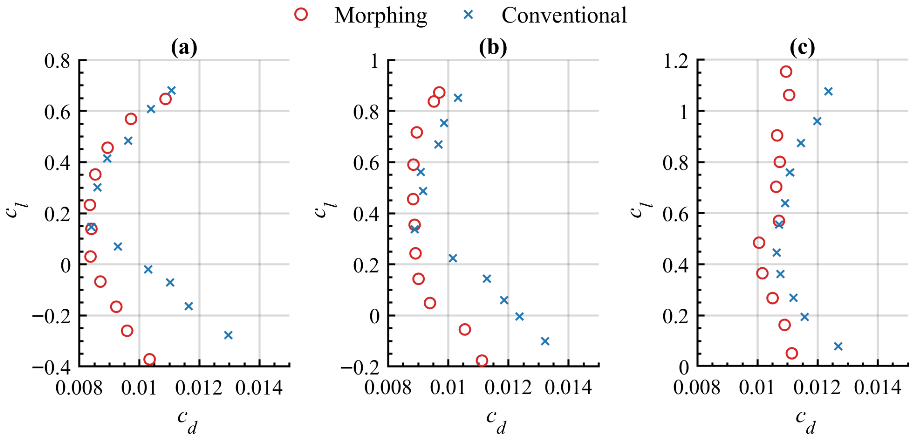

Figure 16. Lift to drag dependency at different flap and trailing-edge deflections from −0.05*c* to 0.05*c* in steps of 0.01*c*: (**a**) At 0° angle of attack, (**b**) At 2° angle of attack, (**c**) At 4° angle of attack.

4. Discussion

The presented algorithm demonstrates that a simple, low-fidelity approach can generate compliant structures. In the worst case, the average deviation of the generated structures when actuated to achieve the optimized shape was just 0.1% of the chord length, while in most two-shape optimizations it ranged between 0.04% and 0.08%. For single-shape optimization, the deviation was as low as 0.023%. In general, larger trailing-edge sections are easier to optimize, as they provide more space for adjustments to achieve the intended shape.

In the second investigated case, with a small 0.26 m chord wing, the trailing-edge optimization structure thickness boundaries were constrained by a relatively large minimum thickness. Although stiffness and strength requirements could be met, manufacturing limitations became the bottleneck in this case, as the structures were defined to be manufactured using an FDM printer.

Selecting different boundaries and parameters, such as the number of support structures or control points, may lead to improved results, as the performance of this approach is highly dependent on the chosen settings. Nevertheless, the presented results are comparable to, or even better than, the outcomes reported by other researchers who optimized only a single shape, indicating strong potential for this method. However, the penalty-based method with predefined weights for multiple objectives can sometimes produce uneven results between both geometries. Ideally, the algorithm would minimize the discrepancy between both geometries evenly, but this is not always achievable. As shown in the results, some optimizations yield lower discrepancies for one shape while the other performs worse, whereas in cases where the optimization converges easily, both geometries can be achieved with similar accuracy. This method could be improved in the future by adopting a more explicitly multi-objective approach that relies less on predefined penalties. Such research is planned for further algorithm investigations.

Using this low-fidelity method, simple morphing wings can be designed and manufactured with modern FDM printing technologies. However, researchers aiming to use FDM for compliant structures must consider that FDM-printed side surfaces are uneven: even when the outer surface appears continuous, it consists of semi-circular ridges with slight bulging, formed by individual printed rasters layered on top of each other. These rasters tend to bulge slightly and can significantly affect the second moment of area at low thicknesses. In this work, cross-sectional characteristics were modeled based on printer settings, which substantially improved the accuracy of the printed structures' shape during morphing, as such discrepancies were not initially apparent. Figure 17 compares section properties between the rectangle and the approximated modeled section geometry as the printed layer count increases towards a thicker beam. The same figure also includes an SEM photo of a multilayer, vertically printed 3D sample. The results show that when the number of layers is small, surface geometry plays a significant role in bending stiffness. Most differences arise from textured surfaces and bulged circular cross-section areas. As the thickness decreases, the textured surface shifts closer to the neutral line of the beam, reducing the amount of material near the edges. In the present morphing trailing edge example, the layer count ranged from 2 to 10, indicating a substantial effect for the outcome.

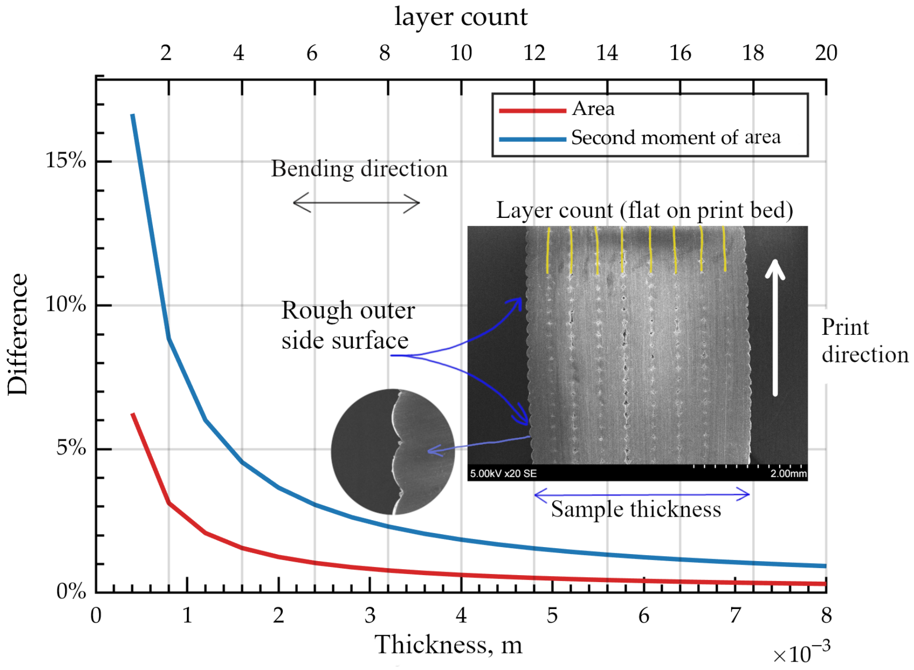

Figure 17. Comparison of section properties between a rectangular beam and a beam with semi-circular bulges on both outer surfaces, based on a 3D-printed cross-section with 0.4 mm layer width and 0.2 mm layer height. SEM pictures displayed together are only of lustration purpose.

When analyzing the 3D-printed wing in the wind tunnel, it was not possible to directly verify whether the optimized geometry was achieved, as the optimization relied on aerodynamic loading and thus the geometry is only realized under those conditions. Variations in aerodynamic shape or flow conditions can alter the outcome, which may explain the wider discrepancy observed between experimental and CFD results. Although some differences could have arisen from initial shape discrepancy, CFD model inaccuracies or wind tunnel setup, the overall outcome was still positive. Direct comparison between conventional flap and morphing trailing edge mitigated some systematic errors, making the results evident. It should be noted that compliant structures are limited in the number of aerodynamic configurations they can achieve with a single actuation strategy. In this work, the optimization considered only one flight condition, and the results under this loading were favorable. Encouraged by these outcomes, the actuated morphing trailing-edge performance was also evaluated at different angles of attack, resulting in slightly different aerodynamic loading cases than those used during optimization, and showing similarly positive results. This suggests that compliant morphing structures can still provide benefits even when the achieved shape deviates slightly from the optimized one. Additionally, at the tested wing scale and velocities, aerodynamic loading likely had a limited effect on structural deformation. Larger velocity variations and a wider range of angles of attack could introduce further limitations for compliant trailing-edge design, indicating that stiffer structures with higher actuation forces might be more effective, though less practical.

5. Conclusions

The paper presents a low-fidelity algorithm for generating compliant, morphing trailing structures using parameterization. The investigation of the algorithm confirms that a low-fidelity optimization approach can effectively produce compliant morphing trailing edge designs. Single-shape optimization achieved very high shape accuracy, whereas the introduction of multiple target shapes reduced its performance outcomes. However, shape deviations remained within acceptable limits and, in several instances, were close to typical manufacturing error margins. Larger trailing-edge sections proved more favorable for optimization due to the greater available adjustment space, while small chord configurations were primarily limited by manufacturing constraints. Using the presented algorithm, a test wing with a morphing trailing edge was manufactured and evaluated through wind tunnel testing. With an optimized morphing trailing edge, c_l/c_d improved by 12.4% compared to the conventional flap, demonstrating that the algorithm effectively improved aerodynamic performance.

Author Contributions: Conceptualization, M.L.; methodology, M.L.; software, M.L.; validation, M.L. and V.L.; resources, M.L. and V.L.; writing—original draft preparation, M.L.; writing—review and editing, M.L. and V.L.; visualization, M.L.; supervision, V.L. All authors have read and agreed to the published version of the manuscript.

Funding: This research received no external funding.

Institutional Review Board Statement: Not applicable.

Informed Consent Statement: Not applicable.

Data Availability Statement: The data that support the findings of this study are available from the corresponding author upon request.

Conflicts of Interest: The authors declare no conflicts of interest.

Abbreviations

The following abbreviations are used in this manuscript:

BESO	Bi-directional Evolutionary Structural Optimization
CFD	Computational Fluid Dynamics
FEM	Finite Element Method
FDM	Fused Deposition Modeling
GA	Genetic algorithm
SEM	Scanning Electron Microscope
SST	Shear Stress Transport
TLBO	Teaching Learning based Optimization
PSO	Particle Swarm Optimization
MPE	Maximum Permissible Error

References

1. Barbarino, S.; Bilgen, O.; Ajaj, R.M.; Friswell, M.I.; Inman, D.J. A Review of Morphing Aircraft. *J. Intell. Mater. Syst. Struct.* **2011**, *22*, 823–877. [CrossRef]
2. Chu, L.; Li, Q.; Gu, F.; Du, X.; He, Y.; Deng, Y. Design, modeling, and control of morphing aircraft: A review. *Chin. J. Aeronaut.* **2022**, *35*, 220–246. [CrossRef]
3. Tavares, S.M.O.; Gamboa, P.V.; de Castro, P.M.S.T. Aircraft Wings and Morphing–Evolution of the Concepts. *Encyclopedia* **2025**, *5*, 101. [CrossRef]
4. Mowla, M.N.; Asadi, D.; Durhasan, T.; Jafari, J.R.; Amoozgar, M. Recent advancements in morphing applications: Architecture, artificial intelligence integration, challenges, and future trends-a comprehensive survey. *Aerosp. Sci. Technol.* **2025**, *161*, 110102. [CrossRef]
5. Jensen, P.D.L.; Wang, F.; Dimino, I.; Sigmund, O. Topology Optimization of Large-Scale 3D Morphing Wing Structures. *Actuators* **2021**, *10*, 217. [CrossRef]
6. Concilio, A.; Galasso, B.; Ameduri, S. Scaling Effects on Morphing Structures: Preliminary Guidelines for Managing the Effects on a Case Study. *Actuators* **2023**, *12*, 366. [CrossRef]
7. Cramer, N.B.; Cellucci, D.W.; Formoso, O.B.; Gregg, C.E.; Jenett, B.E.; Kim, J.H.; Lendraitis, M.; Swei, S.S.; Trinh, G.T.; Trinh, K.V.; et al. Elastic shape morphing of ultralight structures by programmable assembly. *Smart Mater. Struct.* **2019**, *28*, 055006. [CrossRef]

8. Parancheerivilakkathil, M.S.; Ajaj, R.M.; Khan, K.A. A compliant polymorphing wing for small UAVs. *Chin. J. Aeronaut.* **2020**, *33*, 2575–2588. [CrossRef]
9. Wang, Z.; Sun, X.; Yang, Y.; Ge, W.; Li, D.; Xiang, J.; Bao, P.; Wu, Q.; Da Ronch, A. Design optimization and testing of a morphing leading-edge with a variable-thickness compliant skin and a closed-chain mechanism. *Chin. J. Aeronaut.* **2024**, *37*, 285–300. [CrossRef]
10. De Gaspari, A.; Cavalieri, V.; Ricci, S. Experimental and performance validation of a full-scale morphing droop nose design based on composite compliant structures. *Compos. Struct.* **2024**, *348*, 118502. [CrossRef]
11. Mkhoyan, T.; Thakrar, N.R.; De Breuker, R.; Sodja, J. Morphing wing design using integrated and distributed trailing edge morphing. *Smart Mater. Struct.* **2022**, *31*, 125025. [CrossRef]
12. Ameduri, S.; Galasso, B.; Noviello, M.C.; Dimino, I.; Concilio, A.; Catalano, P.; D'Aniello, F.A.; Carossa, G.M.; Pinazo, L.; Derry, J.; et al. Design and Optimization of a Compliant Morphing Trailing Edge for High-Lift Generation. *Appl. Sci.* **2025**, *15*, 2529. [CrossRef]
13. Lu, K.J.; Kota, S. Parameterization Strategy for Optimization of Shape Morphing Compliant Mechanisms Using Load Path Representation. *Proc. Pap.* **2003**, *2*, 693–702. [CrossRef]
14. Gaspari, A.D.; Ricci, S. A Two-Level Approach for the Optimal Design of Morphing Wings Based on Compliant Structures. *J. Intell. Mater. Syst. Struct.* **2011**, *22*, 1091–1111. [CrossRef]
15. Yago, D.; Cante, J.; Lloberas-Valls, O.; Oliver, J. Topology Optimization Methods for 3D Structural Problems: A Comparative Study. *Arch. Comput. Methods Eng.* **2022**, *29*, 1525–1567. [CrossRef]
16. Zhang, Z.; Song, C.; Yang, C.; Cavalieri, V.; Gaspari, A.D.; Ricci, S. Combining Density-based Approach and Optimization Refinement in the Design of Morphing Airfoil Structures. In Proceedings of the AIAA Scitech 2020 Forum, Orlando, FL, USA, 6–10 January 2024. [CrossRef]
17. Zhang, Z.; De Gaspari, A.; Ricci, S. Comparison Between Density-Based And Load-Path-based Method In Various Camber Aerofoil Design. In Proceedings of the 25th Conference of the Italian Association of Aeronautics and Astronautics (AIDAA 2019), Rome, Italy, 9–12 September 2019; Marchetti, M., Ed.; pp. 1–8.
18. Fasel, U.; Keidel, D.; Baumann, L.; Cavolina, G.; Eichenhofer, M.; Ermanni, P. Composite additive manufacturing of morphing aerospace structures. *Manuf. Lett.* **2020**, *23*, 85–88. [CrossRef]
19. Moulton, B.; Hunsaker, D.F. 3D-Printed Wings with Morphing Trailing-Edge Technology. In Proceedings of the AIAA Scitech 2021 Forum, Virtual, 19–21 January 2021. [CrossRef]
20. Jia, S.; Zhang, Z.; Zhang, H.; Song, C.; Yang, C. Wind Tunnel Tests of 3D-Printed Variable Camber Morphing Wing. *Aerospace* **2022**, *9*, 699. [CrossRef]
21. Tong, X.; Ge, W.; Yuan, Z.; Gao, D.; Gao, X. Integrated design of topology and material for composite morphing trailing edge based compliant mechanism. *Chin. J. Aeronaut.* **2021**, *34*, 331–340. [CrossRef]
22. Noviello, M.C.; Dimino, I.; Ameduri, S.; Concilio, A. Conceptual Design and Topology Optimization of a Compliant Morphing Flap for Next Generation Hybrid-Electric Regional Aircraft. In Proceedings of the 34th ICAS Congress, Florence, Italy, 9–13 September 2024; Paper No. ICAS2024-1206.
23. Kambayashi, K.; Kogiso, N.; Watanabe, I.; Yamada, T. Level-set-based topology optimization of a morphing flap as a compliant mechanism considering finite deformation analysis. *Struct. Multidiscip. Optim.* **2023**, *66*, 223. [CrossRef]
24. Zhang, Y.; Ge, W.; Zhang, Z.; Mo, X.; Zhang, Y. Design of compliant mechanism-based variable camber morphing wing with nonlinear large deformation. *Int. J. Adv. Robot. Syst.* **2019**, *16*, 1729881419886740. [CrossRef]
25. Kambayashi, K.; Kogiso, N.; Yamada, T.; Izui, K.; Nishiwaki, S.; Tamayama, M. Multiobjective Topology Optimization for a Multi-layered Morphing Flap Considering Multiple Flight Conditions. *Trans. Jpn. Soc. Aeronaut. Space Sci.* **2020**, *63*, 90–100. [CrossRef]
26. Cavalieri, V.; Gaspari, A.D.; Ricci, S. Aero-Structural Design Optimization of a Morphing Aileron Considering Actuation Aspects. In Proceedings of the AIAA Scitech 2024 Forum, Orlando, FL, USA, 8–12 January 2024; pp. 1–17; AIAA 2024-2113. [CrossRef]
27. Modified Akima Piecewise Cubic Hermite Interpolation-MATLAB Makima-MathWorks Mathworks.com. Available online: https://mathworks.com/help/matlab/ref/makima.html (accessed on 21 May 2025).
28. Rangel, R. Numerical Analysis of Trusses and Frames (NUMA-TF). 2020. Available online: https://gitlab.com/rafaelrangel/numa-tf (accessed on 31 January 2025).
29. Kuipers, T.; Doubrovski, E.L.; Wu, J.; Wang, C.C. A Framework for Adaptive Width Control of Dense Contour-Parallel Toolpaths in Fused Deposition Modeling. *Comput.-Aided Des.* **2020**, *128*, 102907. [CrossRef]
30. Rahman, K.M.; Letcher, T.; Reese, R. Mechanical Properties of Additively Manufactured PEEK Components Using Fused Filament Fabrication, Vol. Volume 2A: Advanced Manufacturing. In Proceedings of the ASME International Mechanical Engineering Congress and Exposition, Houston, TX, USA, 13–19 November 2015. [CrossRef]
31. Perry, B. Theodorsen's and Garrick's Flutter Calculations: Revisited. *J. Aircr.* **2025**, *62*, 224–228. [CrossRef]

32. Pilakkadan, J.S.; Ajaj, R.M.; Haider, Z.; Amoozgar, M. On the Aeroelasticity of a Cantilever Wing Equipped with the Spanwise Morphing Trailing Edge Concept. *Aerospace* **2023**, *10*, 809. [CrossRef]
33. Lendraitis, M.; Lukoševičius, V. Novel Approach of Airfoil Shape Representation Using Modified Finite Element Method for Morphing Trailing Edge. *Mathematics* **2023**, *11*, 1986. [CrossRef]
34. Drela, M. Pros&Cons of Airfoil Optimization. In *Frontiers of Computational Fluid Dynamics*; World Scientific Pub Co Inc.: Hackensack, NJ, USA, 1998; pp. 363–381. [CrossRef]